

Control of chiral orbital currents in a colossal magnetoresistance material

Yu Zhang¹, Yifei Ni¹, Hengdi Zhao¹, Sami Hakani², Feng Ye³, Lance DeLong⁴, Itamar Kimchi^{2*}

and Gang Cao^{1*}

¹*Department of Physics, University of Colorado at Boulder, Boulder, CO 80309, USA*

²*School of Physics, Georgia Institute of Technology, Atlanta, GA 30332, USA*

³*Neutron Scattering Division, Oak Ridge National Lab, Oak Ridge, TN 37831, USA*

⁴*Department of Physics and Astronomy, University of Kentucky, Lexington KY 40506, USA*

Abstract Colossal magnetoresistance (CMR) is an extraordinary enhancement of the electric conductivity in the presence of a magnetic field. It is conventionally associated with a field-induced spin polarization, which drastically reduces spin scattering and thus electric resistance. However, ferrimagnetic $\text{Mn}_3\text{Si}_2\text{Te}_6$ is an intriguing exception to this rule: it exhibits a 7-order-of-magnitude reduction in ab -plane resistivity with a 13-Tesla anisotropy field which occur only when a magnetic polarization is avoided [1]. Here we report an exotic quantum state that is driven by ab -plane chiral orbital currents (COC) flowing along edges of MnTe_6 octahedra. The c -axis orbital moments of ab -plane COC couple to the ferrimagnetic Mn spins to drastically increase the ab -plane conductivity (CMR) when an external magnetic field is aligned along the magnetic hard c -axis. Both the COC state and its CMR are extraordinarily susceptible to small DC currents exceeding a critical threshold, and a hallmark of this COC state is an exotic time-dependent, bistable switching mimicking a first-order “melting” transition. The control of the COC-enabled CMR and bistable switching offers a fundamentally new paradigm for quantum technologies.

* gang.cao@colorado.edu; ikimchi3@gatech.edu

Introduction A necessary characteristic of all known colossal magnetoresistance (CMR) materials is an alignment of magnetic spins that drastically reduces electron scattering, thus electric resistance [2-10]. However, ferrimagnetic $\text{Mn}_3\text{Si}_2\text{Te}_6$ is an intriguing exception to this rule, in that the *ab*-plane electric resistivity is reduced by up to 7 orders of magnitude only when a magnetic field H is applied along the magnetic hard *c*-axis or when a saturated magnetic state is absent [1]. In contrast, the *ab*-plane resistivity decreases by only 20% at most when the magnetization is saturated by H aligned with the magnetic easy *a*-axis (or *ab*-plane) (**Figs.1a-1b**). The data in **Fig. 1b** also reveal a large anisotropy field of at least 13 T. This observation is equally intriguing because magnetic anisotropy is usually a result of spin-orbit coupling; but here the orbital momentum is zero for the Mn^{2+} ($3d^5$) ion with a half-filled $3d$ orbital. This behavior signals a new type of CMR, which has since been confirmed [11], with a peculiar anisotropy that defies existing precedents [2-10] and indicates a novel quantum state that has yet to be identified and understood.

Herein we report extensive evidence of a novel quantum state in $\text{Mn}_3\text{Si}_2\text{Te}_6$: The new state is defined by its unconventional CMR, anisotropy and extraordinary response to application of small DC currents I , including a first-order transition with bistable switching. The switching consists of an abrupt jump in voltage V which takes seconds or minutes to occur after application of a small current to the sample without further stimulus. This time delay and voltage jump drastically increase when H is oriented along the magnetic hard *c*-axis where the CMR occurs [1] but are otherwise absent. Applying $H \parallel c$ -axis also induces a surprising DC tunneling behavior that features $\Delta V/\Delta I = 0$. In short, this state becomes highly conducting (CMR) and resilient when $H \parallel c$ -axis is employed but is insulating and “melts” (mimicking an ice-to-water phase transition) via first-order bistable switching when a small DC current exceeding a certain threshold is applied.

Each of the key phenomena, i.e., the CMR, magnetic anisotropy, and bistable switching, defies conventional wisdom and models; the *simultaneous* occurrence of all these phenomena indicates that a novel paradigm is required to understand the physics of the underlying state. Here we argue that these phenomena can be explained in terms of a state of intra-unit-cell, *ab*-plane chiral orbital currents (COC) that generate net *c*-axis orbital magnetic moments (M_{COC}) which couple with the simultaneously ferrimagnetically ordered Mn spins (M_{Mn}) (**Fig. 1e-1f**). Below the Curie temperature $T_{\text{C}} = 78$ K, the *ab*-plane COC circulate along Te-Te edges of the MnTe_6 octahedra, thereby producing net M_{COC} primarily oriented along the *c*-axis (**Fig. 1e**). M_{COC} arising from Te-orbitals are necessarily coupled with M_{Mn} , giving rise to an unusual spin-orbit coupling that explains the observed large anisotropy field (**Fig. 1b**). Therefore, the observed magnetization results from local M_{Mn} and M_{COC} . Application of $H \parallel c$ -axis can thereby amplify the *ab*-plane COC and M_{COC} and underpins the CMR (**Fig. 1a**). The COC state, Ψ_{C} , is exceedingly sensitive to application of small DC currents I and converts to a trivial state, Ψ_{T} , via first-order, bistable switching when $I > 2$ mA. The rigid coupling of the COC to the Te sublattice and M_{Mn} causes Ψ_{C} to remain metastable over long time scales set by Te atomic motion (as opposed to only electrons or Mn spins which respond on picosecond time scales [12]). Consequently, the bistable switching or melting of Ψ_{C} requires *seconds or minutes* to occur after initial application of a small I to the sample. Our observed temperature-current-field (T-I-H) phase diagram (**Fig.1g**) shows that Ψ_{C} exists under a sheet in T-I-H space that expands with increasing $H \parallel c$ -axis.

A COC state was initially proposed and investigated in studies of high- T_{C} cuprates [13-20] and was later invoked in investigations of other materials, such as iridates [21-23] and Kagome superconductors [24, 25]. A more recent study reports a transport signature of loop current in a Kagome metal [26]; the data show the signal in a charge-ordered phase of the material, which is

attributed a loop-current phase with spontaneously broken mirror symmetries [26]. It is increasingly clear that COC may be widespread beyond the forementioned materials [18, 24-27]. However, no macroscopic transport phenomena attributed to COC that coexist with a long-range magnetic order such as those observed in this work have ever been reported. The signature of COC coupled with long-range magnetic order can be particularly subtle because mirror and time reversal symmetries are already broken, but effects of COC can be exotic and strong. Indeed, the observed CMR [1, 11], magnetic anisotropy and time-dependent bistable switching are both rare and striking. In the following we present the first-such experimental evidence, and then discuss how COC can adequately account for the observations [28].

Crystal and magnetic structures $\text{Mn}_3\text{Si}_2\text{Te}_6$ crystallizes in a trigonal space group $P\bar{3}1c$ (No. 163) with two inequivalent Mn sites, Mn1 and Mn2 [29], forming a *trimer-honeycomb lattice* (**Figs.1e-1f**). It orders ferrimagnetically at $T_C = 78$ K [29, 30] with the Mn spins antiferromagnetically coupled along the c -axis [1]. Recent neutron diffraction data reveal a noncollinear magnetic structure below T_C , in which the Mn spins lie predominantly within the ab -plane, but tilt both within the ab -plane and toward the c -axis by 10° under ambient conditions (**Fig. 1d**) [31]. Application of $H \parallel c$ -axis causes a *gradual* tilting of the spins toward the c -axis while retaining the underlying antiferromagnetic configuration along the c -axis [31], which reinforces a key point that any models based on the Mn spins alone cannot explain the CMR that is also current sensitive.

Structural, transport, and magnetic properties in magnetic fields The a -axis resistivity ρ_a and the c -axis resistivity ρ_c both rise rapidly below T_C , reaching values as high as $10^7 \Omega\text{-cm}$ (**Fig. 1a**) [1]. The a -axis magnetization M_a readily saturates to a value $M_s = 1.56 \mu_B/\text{Mn}$ for $\mu_0 H_{\parallel a} > 0.05$ T, indicating the magnetic easy a -axis (red dashed line in **Fig. 1b**). In contrast, the c -axis magnetization M_c cannot fully attain the a -axis value, even for $\mu_0 H \geq 13$ T (blue dashed line in

Fig. 1b) [1]. Such a large anisotropy field (> 13 T) is conventionally unexpected because the spin-orbit coupling for the Mn^{2+} ($3d^5$) ions is expected to be negligible, which suggests a novel type of spin-orbit coupling may be at play in $\text{Mn}_3\text{Si}_2\text{Te}_6$. Moreover, the measured average magnetic moments for Mn1 and Mn2 are 4.55 and $4.20 \mu_B$, respectively [31], which are significantly smaller than $5 \mu_B$ anticipated for Mn^{2+} ($3d^5$) and suggest that the measured moments may result from partial cancellation between M_{Mn} and M_{COC} . Accordingly, an upper limit of M_{COC} could be on the order of $0.1 \mu_B$ [28].

Further clues can be gained from the observed magnetostriction data that indicate the a -axis undergoes a significant expansion $\Delta a/a$ when $H \parallel c$ -axis but remains essentially unchanged when $H \parallel a$ -axis (**Fig. 1c**), which indicates a strong, anisotropic coupling of H to the lattice. In other words, increasing $H \parallel c$ -axis favors an increase of orbital area and a strong c -axis magnetoelastic coupling. The magnetostriction is relatively easy to associate with orbital moments of a COC state because the Lorentz force acts to expand an ab -plane loop current circulating on the rigid Te-Te edges of MnTe_6 octahedra when $H \parallel c$ -axis. The net orbital magnetization, which equals the loop current times the orbital area, naturally increases due to increasing the orbital area. It is also noteworthy that Ge doping that enhances the CMR also expands the ab -plane, whereas Se doping that weakens the CMR shrinks the ab -plane [28]. We conclude a strong, anisotropic magnetoelastic coupling is consistent with the presence of a COC state, as we further discuss below.

Transport and magnetic properties with small DC currents ρ_a at $H = 0$ is reduced by up to 6 orders of magnitude when applied current I is increased from 10 nA to 10 mA at low temperatures (**Fig. 2a**). T_C rapidly decreases with increasing $I \parallel a$ -axis (and c -axis [28]) (**Fig. 2b**). Specifically, T_C decreases from 83 K at $1 \mu\text{A}$ to 22 K at 1.8 mA, and eventually vanishes at 2 mA (**Fig. 2b**). M_c behaves similarly with increasing $I \parallel a$ -axis (**Fig. 2c**). Clearly, T_C evolves into a first-order

transition with increasing I , until completely suppressed for $I \geq 2$ mA. However, the magnitude of ρ_a in the vicinity of T_C remains essentially unchanged (**Fig. 2b**). This behavior suggests that small currents (< 2 mA) hardly affect the spin scattering of electrons near T_C but effectively weaken the spin exchange coupling that drives T_C . (This current-controlled behavior is vastly different from that seen in other systems [32, 33].) In contrast, T_C systematically shifts to higher temperatures with increasing $H \parallel c$ axis (**Fig. 1a**).

Transport properties in magnetic fields and with small DC currents The response of ρ_a to I drastically changes when $H \parallel c$ -axis (**Fig. 2d**). $H \parallel c$ -axis recovers the magnetic order otherwise suppressed by I , and simultaneously reduces ρ_a , leading to a metallic state below T_C for $I \leq 2$ mA. However, for $I > 2$ mA, H only slightly reduces ρ_a , leaving a much weaker conducting state; the CMR is thus no longer present for $I = 5$ and 10 mA, despite $\mu_0 H_{\parallel c} = 14$ T.

Combining the data for $\rho_a(H=0, I)$ in **Fig. 2a** and $\rho_a(H_{\parallel c}=14\text{T}, I)$ in **Fig. 2d** yields the magnetoresistance ratio as a function of I , $[\rho_a(14\text{T}, I) - \rho_a(0, I)]/\rho_a(0, I)$ at 10 K in **Fig. 2e**. Clearly, the CMR occurs only when $I \leq 2$ mA and abruptly disappears when $I > 2$ mA, which closely tracks the current dependence of T_C in **Fig. 2f**. While $H \parallel c$ -axis enables the CMR, applied current $I > 2$ mA weakens and eventually suppresses the ferrimagnetic state, thereby recovering Ψ_T without the CMR. The correspondence exhibited by the transport anomalies is even more evident in the behavior of the I-V characteristics shown below.

The anomalous I-V characteristic The I-V characteristic for $H = 0$ exhibits a first-order transition characterized by a critical current I_C that separates the two distinct states. In addition, there are two onsets of S-shaped negative differential resistance (NDR) [34, 35], $I_{\text{NDR1}} (< I_C)$ and $I_{\text{NDR2}} (> I_C)$ (**Figs. 3a-3b**). The I-V curve bends over at an onset of the first NDR regime at $I = I_{\text{NDR1}}$, above which an increase in I leads to a decrease in V . This first NDR1 regime ends at $I_C = 1.90$ mA,

where an abrupt increase in V occurs, indicating a first-order transition (**Fig. 3b**). This transition at I_C is followed by the second onset of NDR at $I = I_{\text{NDR2}}$ [28].

The magnetic field dependence of the I-V characteristic illustrates a novel type of bistable switching (**Fig. 3c**). Upon the vanishing of I_{NDR1} at $\mu_0 H_{\parallel c} > 3$ T, an extraordinary region emerges with $\Delta V/\Delta I = 0$ for $0 \leq I \leq I_C$ (**Fig. 3d**). Note that at 7 T and 14 T, $V \approx 0$ as I increases from zero to I_C , a behavior strikingly similar to the DC Josephson effect [36] although no superconducting state is involved here (**Figs. 3c-3d**). This region disappears via an abrupt transition at I_C , and a more resistive state emerges at I_{NDR2} (**Figs. 3d**). The phase diagrams in **Figs. 3e-3f** show the first-order transition at I_C as a function of temperature or magnetic field, respectively. Note that I_C behaves entirely differently when $H \parallel a$ -axis [28].

Time-dependent bistable switching A particularly striking and unique feature of this COC state is that the first-order, bistable switching requires a finite time (e.g., seconds or minutes) and occurs without additional stimulus. The a -axis voltage V_a , measured as a function of time t at 10 K, is shown in **Fig. 4**. Each measurement of V_a starts at $t \equiv 0$ when a constant I is applied and continued until $t = 180$ seconds (and 1,800 seconds [28]) has elapsed. For example, when $I \leq 2.030$ mA at $t = 0$, V_a decreases slightly near $t = 1$ second, and then remains constant for the rest of the time of measurements. A current increase of merely 0.25% (i.e., from 2.030 to 2.035 mA) causes V_a to abruptly spike at $t = 9.6$ seconds, with a voltage increase of $\Delta V_a = 0.52$ V, or $\Delta V_a/V_a = 30\%$, and then immediately stabilizes at a constant value (**Fig. 4a**). Further, slight increases of I progressively shorten the delay time for the switching from 9.6 seconds to 1 second. However, the change in V_a or ΔV_a remains essentially the same, at 0.52 V. This protocol indicates that only two discrete states exist, separated by a first-order switching, which persists up to T_C [28].

The switching process takes even longer when $H \parallel c$ -axis (**Fig. 4b**). The switching takes up to 114 seconds to occur at a significantly stronger $I = 3.98$ mA with $\mu_0 H_{\parallel c} = 7$ T, but the switching leads to a much larger voltage increase, $\Delta V_a \simeq 0.99$ or $\Delta V_a/V_a \simeq 2000$ % (**Fig. 4b**).

It is remarkable that the abrupt bistable switching completely vanishes when $H \parallel a$ -axis (**Fig. 4c**). The abrupt switching is instead replaced by a gradual, continuous change in V_a with I . The stark contrast between data in **Fig.4b** for $H \parallel c$ -axis and **Fig.4c** for $H \parallel a$ -axis reinforces the following key points. Application of $H \parallel c$ -axis apparently strengthens Ψ_C via the c -axis M_{CoC} , which interlock with the Te sublattice and M_{Mn} (**Fig. 4e**). It therefore takes a stronger I and a longer t for the charge carriers to alter the current configuration. The fact that this switching is always achieved via a first-order transition further emphasizes the key differences in current paths and orbitals involved in the two states. Conversely, application of $H \parallel a$ -axis, where the CMR is absent, tilts the c -axis M_{CoC} towards the a -axis, which weakens or even destroys Ψ_C (**Fig. 4f**). The continuous increase in V_a with increasing I for $H \parallel a$ -axis suggests that Ψ_C is no longer robust or distinct at $t = 0$. That the data in **Fig. 4c** still bear some resemblance to the data in **Fig. 4b** may imply the existence of a “mixed state” consisting of coexisting Ψ_C and Ψ_T when $H \parallel a$ -axis.

Our extensive measurements further reveal that the critical current for switching is an intrinsic parameter; that is, no switching will happen for any smaller current, no matter how close it is to the critical current and how much time elapses (e.g., 30 minutes [28]). Moreover, $\Delta V_a/V_a$ as a function of $H \parallel c$ -axis is unchanged for all temperatures below 70 K, which demands a bistable state.

Absence of Joule heating Self-heating effects cause a continuous drift in local temperature. They are generally isotropic or diffusive and vary continuously with changing current. Such behavior is ruled out in the present study by (i) the abrupt nature of the switching without any drifting, (ii)

the independence of the two discrete values of V_a on the magnitude of I in **Figs. 4a-4b**, (iii) the extremely anisotropic behavior in **Figs. 4b-4c**, and moreover, (iv) the electric energy $W = V_a \times I \times t$ dissipated by the applied current at each switching, for $H = 0$ and $\mu_0 H_{\parallel c} = 7$ T, *decreases rapidly with increasing I* , which is clearly inconsistent with Joule heating (**Fig. 4d**).

Discussion of the COC state The COC, which couple to the ferrimagnetic state, originate from spontaneous breaking of time-reversal symmetry below $T_C = 78$ K and circulate along Te-Te edges of the MnTe_6 octahedra, producing M_{COC} primarily oriented along the c -axis [28]. (Note that similar orbital moments of loop currents are discussed in the cuprates [19, 37]). In the absence of $H \parallel c$ -axis, the net circulation of the COC is zero. This is because the COC are allowed to circulate both clockwise and counterclockwise (**Figs. 1e, 1f** and **Fig. 5**), resulting in domains with two opposite directions of the COC. The disordered domains lead to strong scattering and high resistance. Application of $H \parallel c$ axis favors only one circulation (i.e., either clockwise or counterclockwise) and enlarges its domains (and concurrently reducing the domains with the opposite circulation). Since the overall conductivity is a sensitive function of the configuration of the COC domains, the alignment of the dominant circulation domains is crucial for the enhancement of Ψ_C by $H \parallel c$ axis, and the sharp reduction in electron scattering evident in the 10^7 -CMR (**Figs. 1a-1b**) [28]. Naturally, application of $H \parallel a$ -axis weakens the c -axis M_{COC} , thus Ψ_C , and necessarily causes suppression of the CMR.

Applying nonequilibrium $I > 2\text{mA}$ weakens the order parameter of Ψ_C , therefore destabilizes Ψ_C in favor of Ψ_T . This is expected since the COC configuration does not permit any net current because each of the four independent parameters that specify Ψ_C [28] forms a circulating current within the unit cell with no net uniform component (**Figs. 5a-5c**). The resistivity is reduced with increased I , but at the same time, the increased I also weakens and eventually

suppresses the ferrimagnetic state, and consequently Ψ_C , leading to a first-order phase transition that destroys Ψ_C (**Figs. 2a-2d**).

The rigid coupling of the COC (and M_{COC}) to the Te sublattice and M_{Mn} is a signature of Ψ_C . The COC extend over multiple atomic sites, with couplings that depend on the ionic positions and dictate the current strength. Therefore, Ψ_C entails a particularly strong coupling between the lattice, the c -axis M_{COC} and M_{Mn} as well as the anisotropic magnetoelastic coupling. Such a rigid coupling in Ψ_C explains the current-driven first-order transition from Ψ_C to Ψ_T (**Figs. 1-4**). This coupling also enables Ψ_C to remain metastable over long time scales that are set by Te atomic motion and bond lengths or fluctuations/phonon effects rather than by electrons and/or Mn spins alone (**Fig.4a**). Application of $H \parallel c$ -axis, via the c -axis M_{COC} , strengthens the coupling, further extending the time scale (**Fig.4b**) but application of $H \parallel a$ -axis weakens or destroys the coupling (**Fig.4c**).

Our observations implicate an exotic quantum state of matter that yields unusual responses to small applied electric currents and magnetic fields. While further work, such as optical control of this state [38], will reveal more insights into the COC, the observed phenomena certainly promise wide-ranging opportunities for fundamental advances in condensed matter physics and future device applications.

Important Notes: The final version of this paper, which is more updated than this version, is to be published in *Nature*. The updated Methods, Extended Data Figures and updated references are presented in the final version of the paper.

References

1. *Colossal magnetoresistance via avoiding fully polarized magnetization in ferrimagnetic insulator $Mn_3Si_2Te_6$* , Yifei Ni, Hengdi Zhao, Yu Zhang, Bing Hu, Itamar Kimchi and Gang Cao, *Letter of Phys. Rev. B* **103**, L161105 (2021).
2. *Colossal magnetoresistance*, A. P. Ramirez, *J. Phys.: Condens. Matter* **9**, 8171 (1997)
3. *Dynamic Jahn-Teller Effect and Colossal Magnetoresistance in $La_{1-x}Sr_xMnO_3$* , A. J. Millis, B. I. Shraiman, and R. Mueller, *Phys. Rev. Lett.* **77**, 175 (1996).
4. *The physics of manganites: Structure and transport*, M. B. Salamon and M. Jaime, *Rev. Mod. Phys.* **73**, 583 (2001).
5. *Nanoscale Phase Separation and Colossal Magnetoresistance*, E. Dagotto, (Springer, Berlin, 2002).
6. *Critical features of colossal magnetoresistive manganites*, Y. Tokura, *Rep. Prog. Phys.* **69**, 797 (2006).
7. *Magnetoresistance in Mn Pyrochlore: Electrical Transport in a Low Carrier Density Ferromagnet*, P. Majumdar and P. Littlewood, *Phys. Rev. Lett.* **81**, 1314 (1998).
8. *Giant magnetoresistance in $Tl_2Mn_2O_7$ with the pyrochlore structure*, Y. Shimakawa, Y. Kubo, and T. Manako, *Nature* **379**, 53 (1996).
9. *Colossal magnetoresistance in a nonsymmorphic antiferromagnetic insulator*, Priscila Rosa, Yuanfeng Xu, Marein Rahn, et al, *npj Quantum Mater* **5**, 52 (2020).
10. *Large negative magnetoresistance in the antiferromagnetic rare-earth dichalcogenide, $EuTe_2$* , Junjie Yin, Changwei Wu, Lisi Li, Jia Yu, Hualei Sun, Bing Shen, Benjamin A. Frandsen, Dao-Xin Yao, and Meng Wang, *Phys. Rev. Mater.* **4**, 013405 (2020).

11. *Colossal angular magnetoresistance in ferrimagnetic nodal-line semiconductors*, J. Seo, C. De, H. Ha, J. E. Lee, S. Park, J. Park, Y. Skourski, E. S. Choi, B. Kim, G. Y. Cho, H. W. Yeom, S.-W. Cheong, J. H. Kim, B.-J. Yang, K. Kim, and J. S. Kim, *Nature* 599, 576 (2021)
12. *Ultrafast electron relaxation in superconducting $\text{Bi}_2\text{Sr}_2\text{CaCu}_2\text{O}_{8+\delta}$ by time-resolved photoelectron spectroscopy*, L. Perfetti, P. A. Loukakos, M. Lisowski, U. Bovensiepen, H. Eisaki, and M. Wolf., *Phys. Rev. Lett.* 99, 197001 (2007)
13. *Theory of the Pseudogap State of the Cuprates*, C. M. Varma, *Phys. Rev. B* 73, 155113 (2006)
14. *Pseudogap in Cuprates in the Loop-Current Ordered State*, C. M. Varma, *J. Phys. Condens. Matter* 26, 505701 (2014).
15. *Proposed Chiral Texture of the Magnetic Moments of Unit-Cell Loop Currents in the Pseudogap Phase of Cuprate Superconductors*, S. S. Pershoguba, K. Kechedzhi, and V. M. Yakovenko, *Phys. Rev. Lett.* 111, 047005 (2013).
16. *Erratum: Proposed Chiral Texture of the Magnetic Moments of Unit-Cell Loop Currents in the Pseudogap Phase of Cuprate*, S. S. Pershoguba, K. Kechedzhi, and V. M. Yakovenko, *Phys. Rev. Lett.* 113, 129901 (2014).
17. *Observation of Orbital Currents in CuO* , V. Scagnoli, U. Staub, Y. Bodenthin, R. A. de Souza, M. García-Fernández, M. Garganourakis, A. T. Boothroyd, D. Prabhakaran, and S.W. Lovesey, *Science* 332, 696 (2011).
18. *Orbital Currents, Anapoles, and Magnetic Quadrupoles in CuO* , S. Di Matteo and M. R. Norman, *Phys. Rev. B* 85, 235143 (2012).
19. *Tilted loop currents in cuprate superconductors*, V. M. Yakovenko, *Physica B* 460, 159(2015).

20. *Loop currents in quantum matter*, Philippe Bourges, Dalila Bounoua and Yvan Sidis, arXiv:2103.13295v2 [cond-mat.str-el] 10 Jul 2021.
21. *Evidence of an odd-parity hidden order in a strongly spin-orbit coupled correlated iridates*, L. Zhao, D. H. Torchinsky, H. Chu, V. Ivanov, R. Lifshitz, R. Flint, T. Qi, G. Cao and D. Hsieh, *Nature Physics* **12**, 32 (2015)
22. *Time-reversal symmetry breaking hidden order in $Sr_2(Ir,Rh)O_4$* , J. Jeong, Y. Sidis, A. Louat, V. Brouet, P. Bourges, *Nature Communications* **8**, 15119 (2017)
23. *Bond Directional Anapole Order in a Spin-Orbit Coupled Mott Insulator $Sr_2Ir_{1-x}Rh_xO_4$* , H. Murayama, K. Ishida, R. Kurihara, T. Ono, Y. Sato, Y. Kasahara, H. Watanabe, Y. Yanase, G. Cao, Y. Mizukami, T. Shibauchi, Y. Matsuda, and S. Kasahara, *Phys. Rev. X* **11**, 011021 (2021)
24. *Unconventional chiral charge order in kagome superconductor KV_3Sb_5* , Yu-Xiao Jiang, Jia-Xin Yin, M. Michael Denner, et al, *Nat. Mater.* **20**, 1353 (2021)
25. *Chiral flux phase in the Kagome superconductor AV_3Sb_5* , Xilin Feng, Kun Jiang, Ziqiang Wang, Jiangping Hu, *Science Bulletin* **66**, 1384 (2021)
26. *Field-tuned chiral transport in charge-ordered CsV_3Sb_5* , Chunyu Guo, Carsten Putzke, Sofia Konyzheva, et al, arXiv:2203.09593v1
27. *Discovery of charge density wave in a correlated kagome lattice antiferromagnet*, Xiaokun Teng, Lebing Chen, Feng Ye, Elliott Rosenberg, Zhaoyu Liu, Jia-Xin Yin, Yu-Xiao Jiang, Ji Seop Oh, M. Zahid Hasan, Kelly J. Neubauer, Bin Gao, Yaofeng Xie, Makoto Hashimoto, Donghui Lu, Chris Jozwiak, Aaron Bostwick, Eli Rotenberg, Robert J. Birgeneau, Jiun-Haw Chu, Ming Yi, Pengcheng Dai, arxiv.org/abs/2203.11467

28. *Supplemental Material* including additional discussion on CMR and COC, data for DC currents applied along the c -axis and time-dependent bistable switching at various temperatures and magnetic fields.
29. *Magnetic order and interactions in ferrimagnetic $Mn_3Si_2Te_6$* , Andrew F. May, Yaohua Liu, Stuart Calder, David S. Parker, Tribhuwan Pandey, Ercan Cakmak, Huibo Cao, Jiaqiang Yan, and Michael A. McGuire, *Phys. Rev. B* **95**, 174440 (2017)
30. *Critical behavior and magnetocaloric effect in $Mn_3Si_2Te_6$* , Y. Liu and C. Petrovic, *Phys. Rev. B* **98**, 064423 (2018).
31. *Magnetic Structure and Spin Fluctuation in Colossal Magnetoresistance Ferrimagnet $Mn_3Si_2Te_6$* , Feng Ye, Masaaki Matsuda, Zachary Morgan, Todd Sherline, Yifei Ni, Hengdi Zhao, and Gang Cao, submitted, 2022
32. *Electrical Control of Structural and Physical Properties via Spin-Orbit Interactions in Sr_2IrO_4* , G. Cao, J. Terzic, H. D. Zhao, H. Zheng, L. E DeLong and Peter Riseborough, *Phys. Rev. Lett* **120**, 017201 (2018)
33. *Nonequilibrium Orbital Transitions via Applied Electrical Current in Calcium Ruthenates*, Hengdi Zhao, Bing Hu, Feng Ye, Christina Hoffmann, Itamar Kimchi and Gang Cao; *Phys. Rev. B* **100**, 241104(R) Rapid Comm (2019)
34. *Emerging memories: resistive switching mechanisms and current status*, Doo Seok Jeong, Reji Thomas, R S Katiyar, J F Scott, H Kohlstedt, A Petraru and Cheol Seong Hwang, *Rep. Prog. Phys.* **75**, 076502 (2012)
35. *Who Wins the Nonvolatile Memory Race?* G.I. Meijer, *Science* **319**, 1625 (2008)
36. *Study of Superconductors by Electron Tunneling*, Ivar Giaever and Karl Megerle, *Phys. Rev.* **122**, 1101 (1961)

37. *Orientation of the intra-unit-cell magnetic moment in the high-Tc superconductor HgBa₂CuO_{4+δ}*, Yang Tang, Lucile Mangin-Thro, Andrew Wildes, Mun K. Chan, Chelsey J. Dorow, Jaehong Jeong, Yvan Sidis, Martin Greven, and Philippe Bourges, Phys. Rev. B 98, 214418 (2018)
38. *Optical control of topological memory based on orbital magnetization*, S. S. Pershoguba and V. M. Yakovenko, Phys. Rev. B 105, 064423 (2022).

Figure Captions

Fig. 1. Physical properties in applied magnetic fields and phase diagram (a) The temperature dependence of the a -axis resistivity ρ_a at various magnetic fields. (b) The magnetic field dependence of the a -axis magnetoresistance ratio $[\rho_a(H)-\rho_a(0)]/\rho_a(0)$ and the magnetization M (dashed lines, right scale) for $H \parallel c$ -axis (blue) and $H \parallel a$ -axis (red). (c) The a -axis magnetostriction $\Delta a/a$ for $H \parallel c$ -axis (blue) and $H \parallel a$ -axis (red). (d) The crystal and magnetic structure [31]; the yellow arrows indicate the ab -plane expansion when $H \parallel c$ -axis denoted by the blue arrow. (e) the COC and corresponding c -axis M_{COC} ; different colors indicate different magnitudes of M_{COC} (see details in Fig.5 and Ref. 28). (f) The ab -plane view of the COC. (g) A T-I-H phase diagram. Note that $H \parallel c$ -axis and $I \parallel a$ -axis. Ψ_C exists under the purple sheet in the T-I-H space and beyond it is Ψ_T .

Fig. 2. Response of physical properties to DC currents and applied magnetic fields: (a) The a -axis resistivity ρ_a at various applied DC currents I for $H = 0$. (b) Enlarged plot of ρ_a in the outlined region in (a). The dashed gray lines highlight the near-constant values of ρ_a at and just below T_C . (c) The c -axis magnetization M_c at various DC currents I along the a -axis for $\mu_0 H = 0.5$ T. Note the first-order transition evident in the ρ_a and M_c data induced by $I = 1.5$ and 1.8 mA.

(d) Temperature dependence of ρ_a at various applied DC currents I for $\mu_0 H = 14$ T. Note that the CMR is absent for $I = 5$ mA and 10 mA. (e) The change of ρ_a for $\mu_0 H = 14$ T and various values of the applied I . (f) T_C at various values of I (generated from data in Figs. 2b-2c). Note that both the CMR and T_C vanish for $I > 2$ mA.

Fig. 3. The a -axis I-V characteristic (a) At various temperatures and $H = 0$; (b) Details of the outlined area in (a); note the first-order transition at I_C . Note that the sudden voltage increase, $\Delta V = V_{\text{NDR2}} - V_C = 0.52$ V, results from a tiny current increase of 0.1 mA from the value of I_C . (c) I-V characteristics for $T = 10$ K and $H \parallel c$ -axis. (d) Details of the outlined area in (c). Note the regime where $\Delta V/\Delta I = 0$ emerges for $\mu_0 H \geq 3$ T, and where $V_a \approx 0$ for $I < I_C$ for $\mu_0 H = 7$ and 14 T, and increasing H leads to an expansion of the region of $\Delta V/\Delta I = 0$. The critical current I_C as well as I_{NDR1} and I_{NDR2} as a function of (e) temperature and (f) magnetic field. Note that I_C is depressed with increasing temperature and eventually vanishes near T_C but is enhanced and remains sharp with increasing $H \parallel c$ -axis.

Fig. 4. Time-dependent bistable switching: (a, b, c) The a -axis voltage V_a as a function of time t at $T = 10$ K for (a) $H = 0$, (b) $\mu_0 H_{\parallel c} = 7$ T and (c) $\mu_0 H_{\parallel a} = 7$ T. (d) The electric energy W due to applied I as a function of I . The schematics for (e) $H \parallel c$ -axis, which couples to and enhances Ψ_C , corresponding to the case in (b) and (f) $H \parallel a$ -axis, which suppresses Ψ_C , corresponding to the case shown in (c). Note c -axis M_{COC} are denoted by the small red and blue arrows in the octahedron.

Fig. 5. COC below T_C The magnetic symmetry group is $C2'/c'$ (No. 15.89, BNS setting) [31], and there are four independent current patterns that preserve the magnetic symmetry group and the crystal space group $P-31c$ (No. 163) [28]. (a) The four-parameter, ferrimagnetic net, non-zero c -axis magnetization. The red, cylindrical arrows are the Mn spins. Four COC are denoted by small

arrows (red, blue, green, and purple). The top view of the Mn1 plane (left) and the side view (right). Details of **(b)** the Mn1 plane and **(c)** the Mn2 plane [28 for more details].

Methods

Single crystals of $\text{Mn}_3\text{Si}_2\text{Te}_6$ were grown using a flux method. Measurements of crystal structures were performed using a Bruker Quest ECO single-crystal diffractometer with an Oxford Cryosystem providing sample temperature environments ranging from 80 K to 400 K. Chemical analyses of the samples were performed using a combination of a Hitachi MT3030 Plus Scanning Electron Microscope and an Oxford Energy Dispersive X-Ray Spectroscopy (EDX). The measurements of the electric resistivity and I-V characteristic were carried out using a Quantum Design (QD) Dynacool PPMS system having a 14-Tesla magnet and a set of external Keithley meters that provides current source and measures voltage with a high precision. The magnetization with electric current was measured using a Quantum Design MPMS-XL magnetometer with a homemade probe. The magnetostriction was measured using a home-made dilatometer compatible with the QD Dynacool PPMS system. The dilatometer is made with four identical KYOWA, type KFL strain gauges forming a Wheatstone bridge with the sample mounted on one arm and the rest three as compensators to cancel unwanted changes in the strain gauges due to changes in temperature and/or magnetic field.

Acknowledgments

This work is supported by National Science Foundation via Grants No. DMR 1903888 and DMR 2204811. The theoretical part of this work is in part performed at Aspen Center for Physics, which is supported by National Science Foundation grant PHY-1607611. The work at ORNL's SNS is sponsored by the Scientific User Facilities Division, Office of Basic Energy Sciences, U.S. Department of Energy. G.C. thanks Minhyea Lee, Rahul Nandkishore, Xi Chen, Michael Hermele,

David Singh, Dmitry Reznik, Daniel Dessau, and Noel Clark for useful discussions. I.K. thanks Erez Berg, Martin Mourigal, Bruno Uchoa, Chandra Varma, and Ziqiang Wang for useful discussions.

Author contributions

Y.Z. conducted measurements of the physical properties and data analysis; Y.F.N. grew the single crystals, characterized the crystal structure of the crystals, measured magnetization with applied currents and contributed to the data analysis; H.D.Z. conducted measurements of crystal and physical properties and data analysis; F.Y. determined the magnetic structure of the crystals using neutron diffraction and contributed to the data analysis; S.H. contributed to the theoretical analysis including detailed configurations of chiral orbital currents presented in the main text and Supplemental Material; L.E.D. contributed to the data analysis and paper writing. I.K. proposed the theoretical argument, formed the theoretical discussion of the paper and contributed to paper writing; G.C. initiated and directed the work, analyzed the data and wrote the paper.

Competing interests

None.

Materials & Correspondence

Professor Gang Cao, gang.cao@colorado.edu

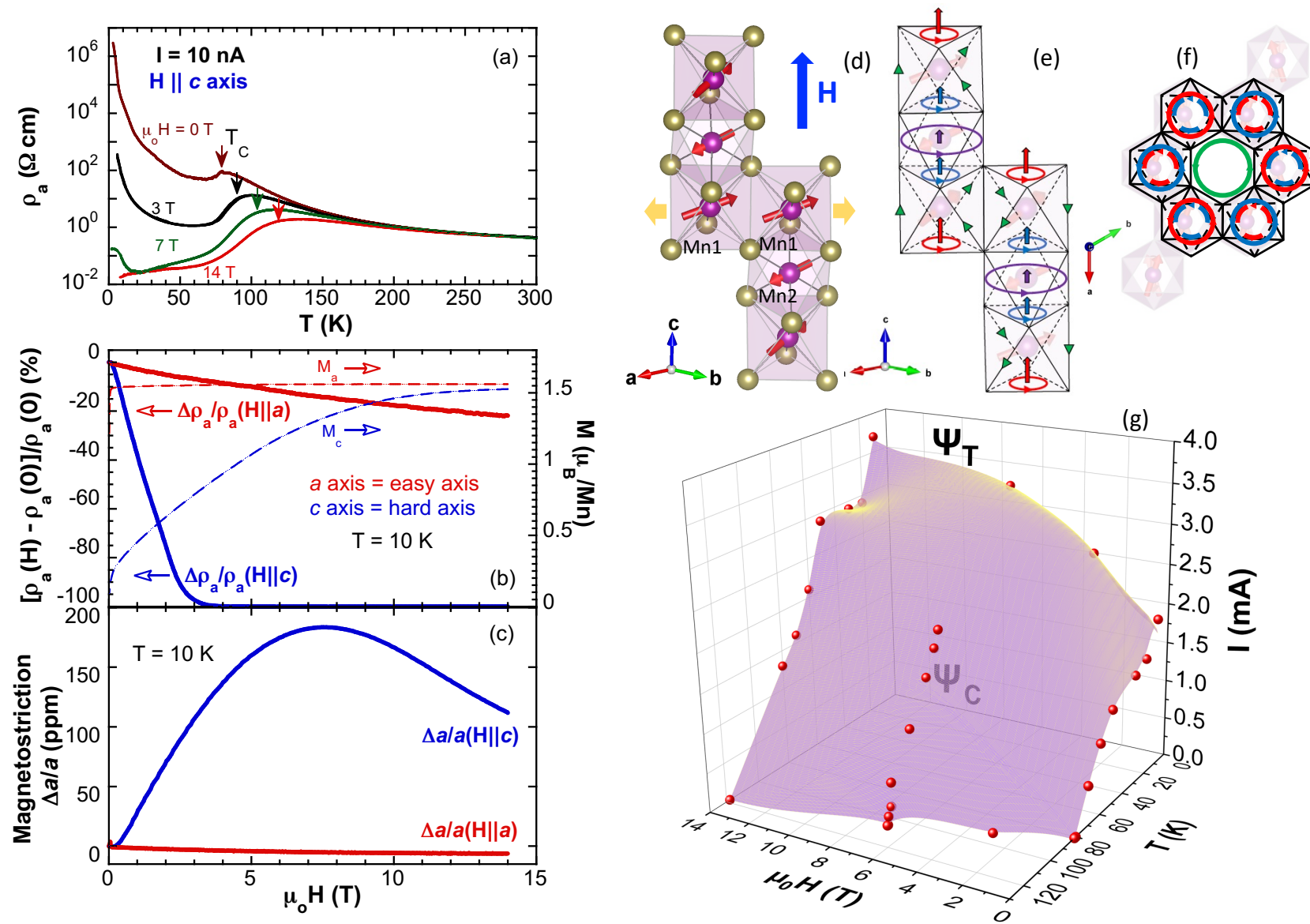


Figure 1

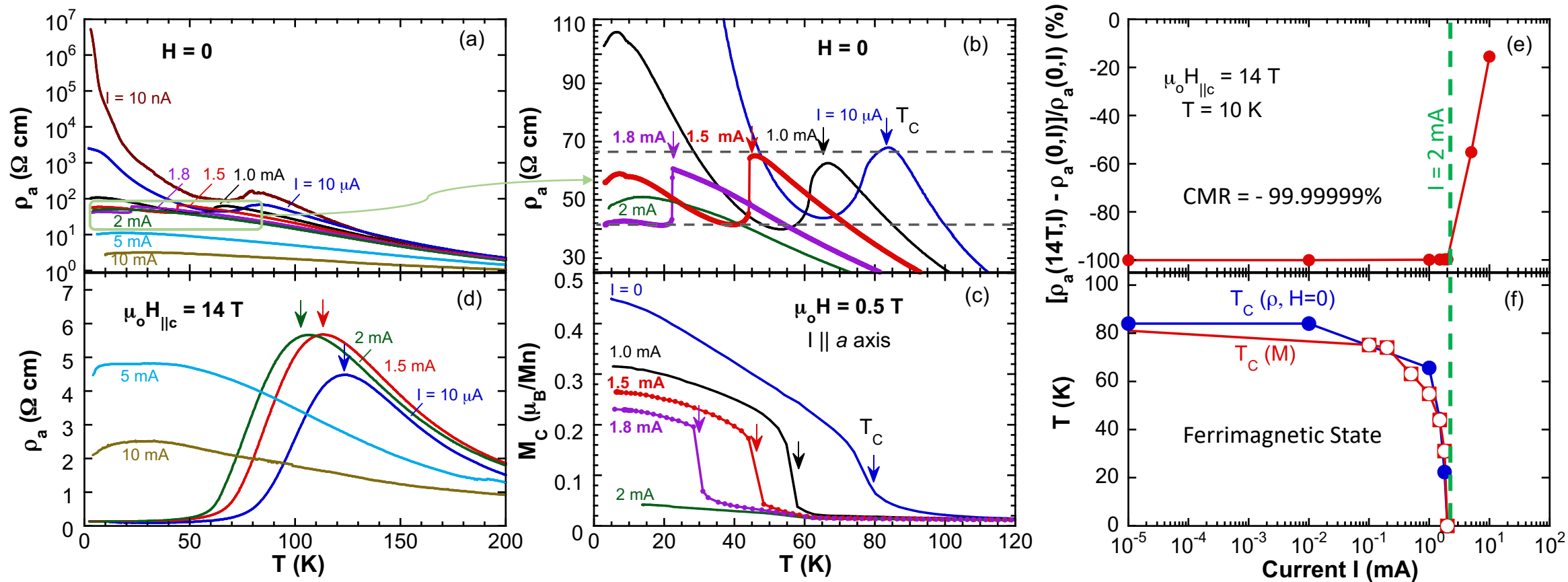


Figure 2

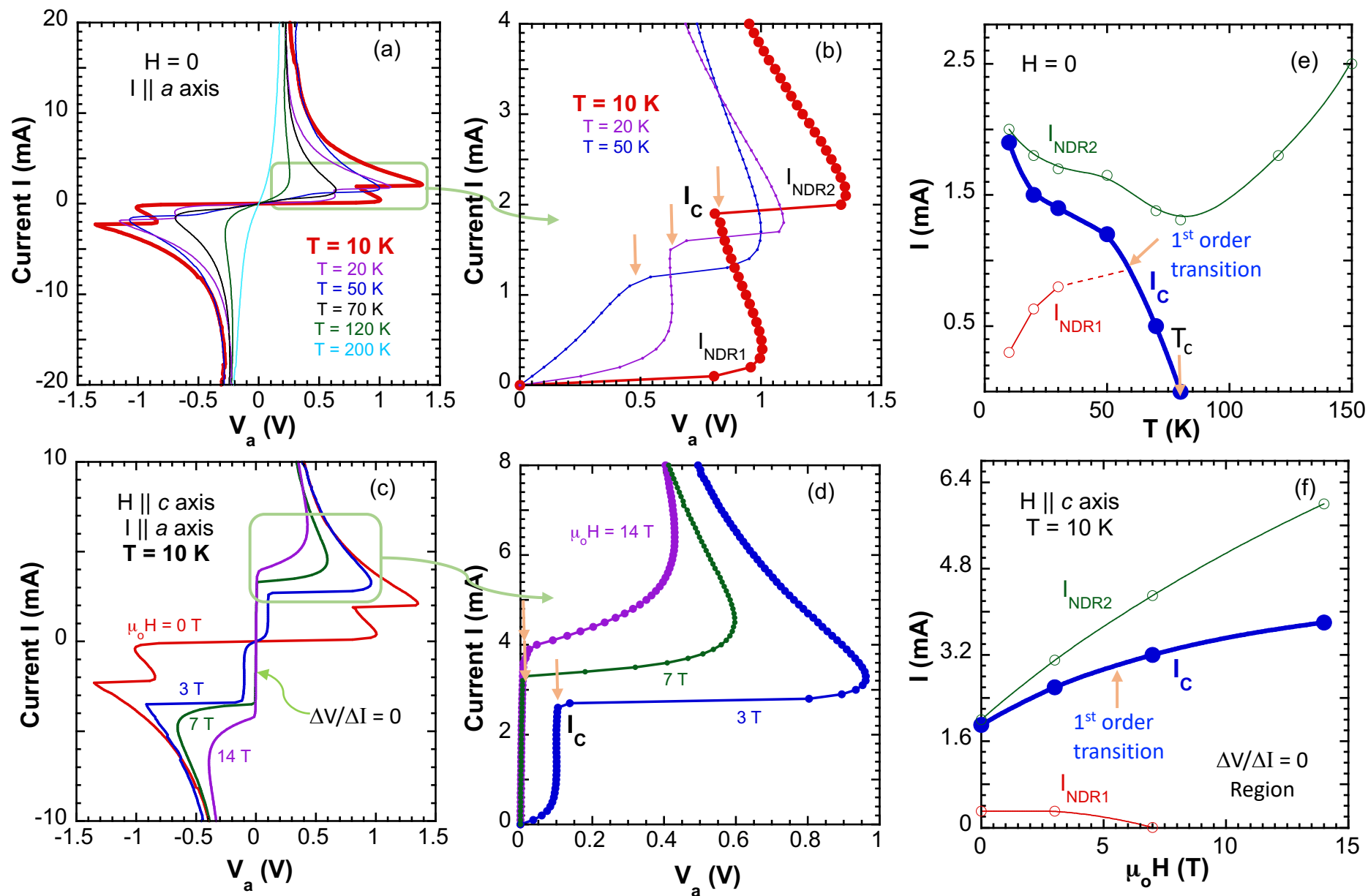


Figure 3

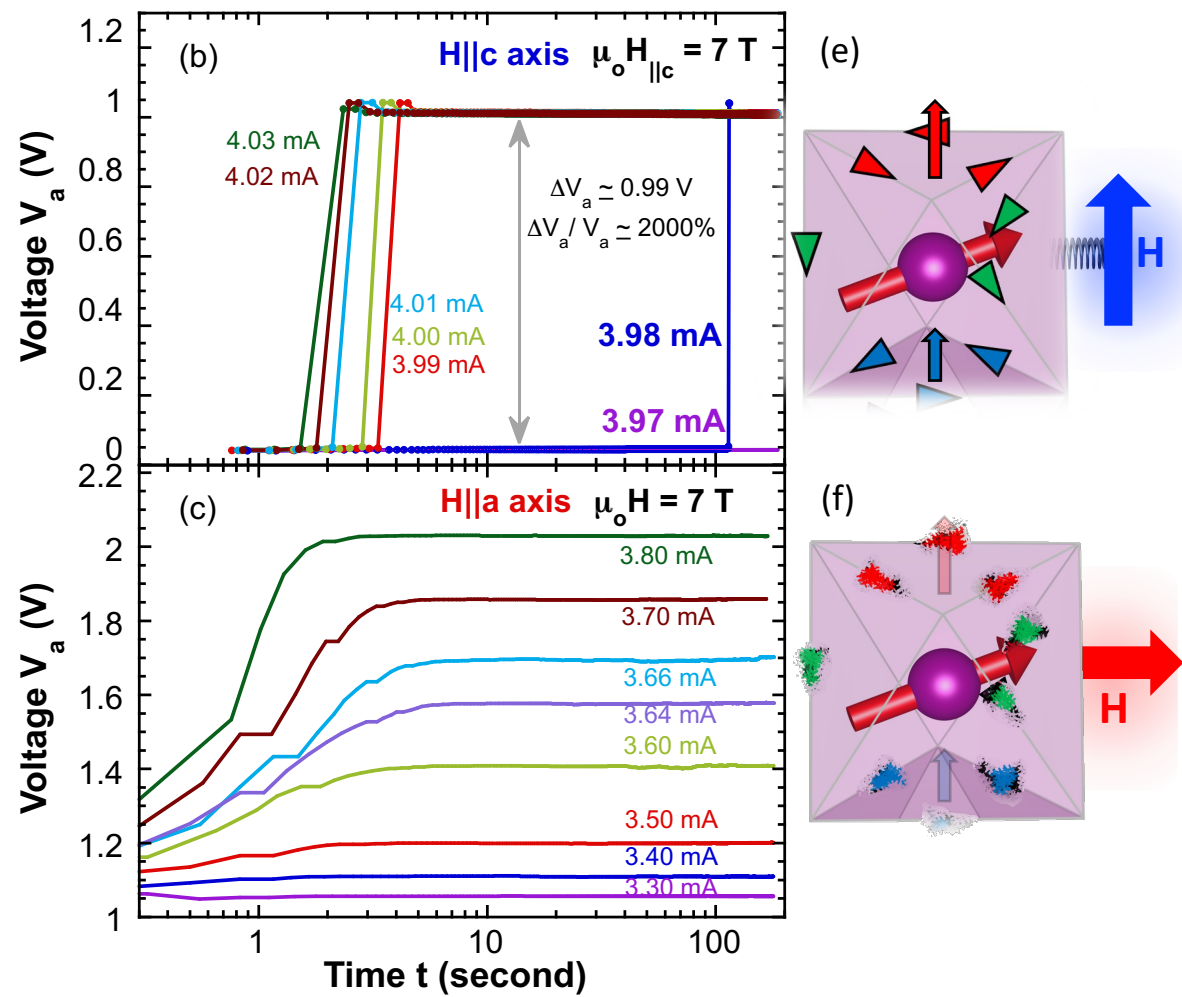
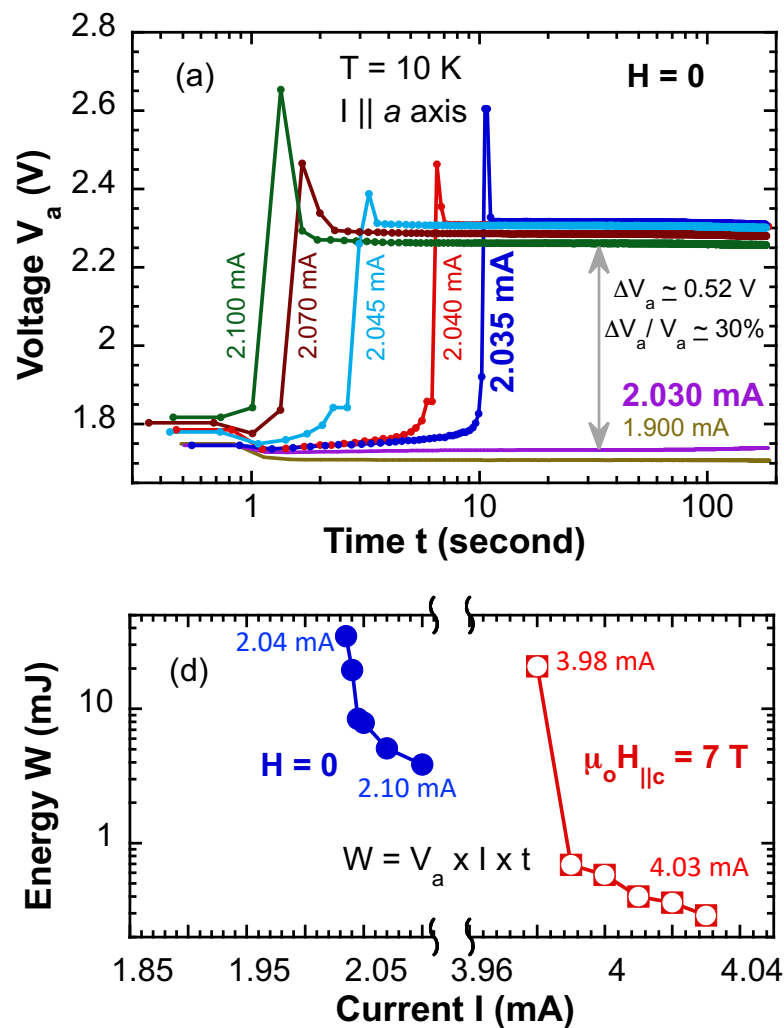


Figure 4

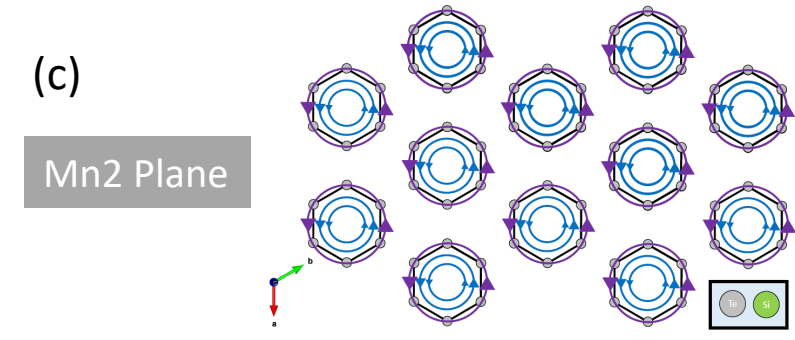
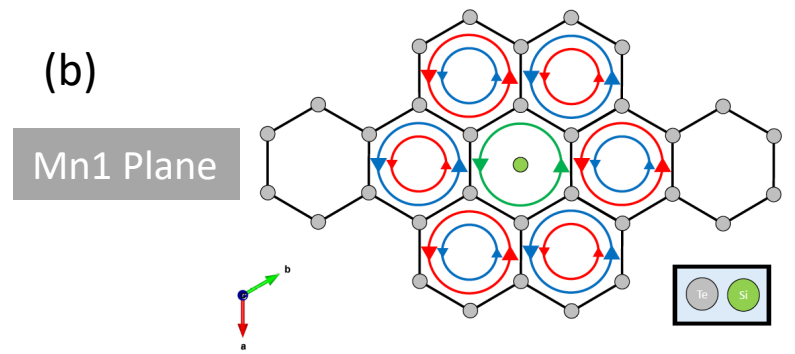
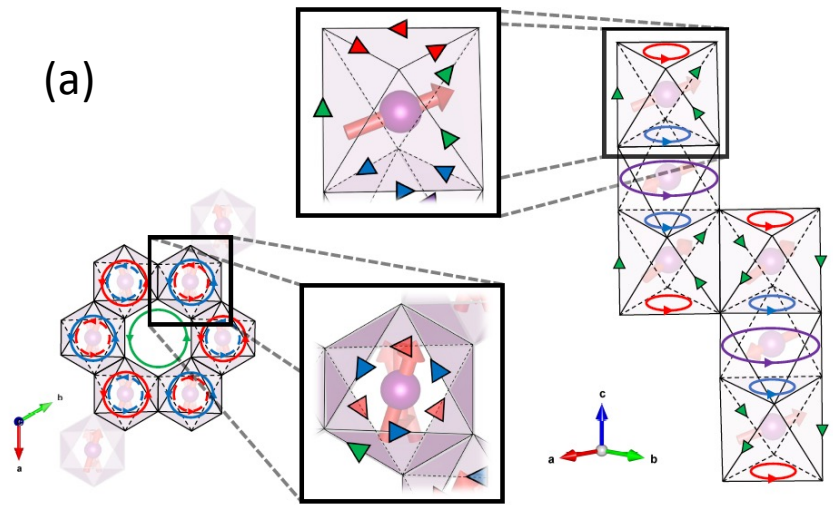


Figure 5

Control of chiral orbital currents in a colossal magnetoresistance material

Yu Zhang¹, Yifei Ni¹, Hengdi Zhao¹, Sami Hakani², Feng Ye³, Lance DeLong⁴, Itamar Kimchi²
and Gang Cao¹

¹*Department of Physics, University of Colorado at Boulder, Boulder, CO 80309, USA*

²*School of Physics, Georgia Institute of Technology, Atlanta, GA 30332, USA*

³*Neutron Scattering Division, Oak Ridge National Lab, Oak Ridge, Tennessee 37831, USA*

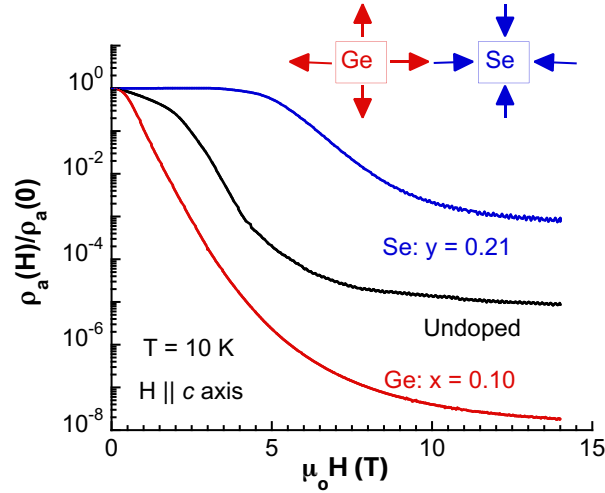
⁴*Department of Physics and Astronomy, University of Kentucky, Lexington KY 40506, USA*

I. Additional notes on the chiral orbital currents, colossal magnetoresistance, and bistable switching in $\text{Mn}_3\text{Si}_2\text{Te}_6$

1. The chiral orbital currents (COC) reported in the main text not only coexist with long range magnetic order but also produce their own nonzero net magnetization. The COC discussed in the cuprates and other materials involve zero net circulation, and zero net magnetic moment; By their observed symmetries, they necessarily entail an “antiferromagnetic” pattern of clockwise and counterclockwise COC circulations. This distinction is key to what makes the COC of this present material unique.
2. It is important to note that colossal magnetoresistance (CMR) is in the lowest order tensor, unlike high-order, non-linear electric response known as electronic magneto-chiral anisotropy (eMChA).
3. We would like to point out that our picture of COC requires strongly correlated physics that are irreconcilable with a picture purely based on electronic bands with a band gap [1]. Our model goes beyond simple modifications of a band structure due to interactions.
4. The CMR is enhanced (**SM-Fig.1**), while the saturated magnetization M_s is reduced to 1.40 μ_B/Mn in $\text{Mn}_3(\text{Si}_{1-x}\text{Ge}_x)_2\text{Te}_6$, which is further evidence that larger orbital moments of the COC state partially cancel the net magnetic moments. On the other hand, in $\text{Mn}_3\text{Si}_2(\text{Te}_{1-y}\text{Se}_y)_6$ the

CMR is weakened (**SM-Fig.1**), but M_s is enhanced up to $1.7 \mu_B/\text{Mn}$, which indicates smaller orbital moments that lie on the mixed-occupancy, chalcogenide sublattice have a weaker cancellation effect.

It is also noteworthy that Ge doping that enhances the CMR also expands the ab -plane, whereas Se doping that weakens the CMR shrinks the ab -plane (Inset in **SM-Fig.1**).



SM-Fig.1. The magnetic field dependence of the a -axis magnetoresistance ratio defined by $\rho_a(H)/\rho_a(0)$ for $\text{Mn}_3(\text{Si}_{1-x}\text{Ge}_x)_2\text{Te}_6$ (red), $\text{Mn}_3\text{Si}_2(\text{Te}_{1-y}\text{Se}_y)_6$ (blue) and undoped compound (black). Inset: schematic illustration of the unit cell expansion and contraction due to Ge doping (red) and Se doping (blue), respectively

5. The orbital magnetic moments due to the COC are estimated based on the total measured moments, 4.55 and 4.20 Bohr magneton for Mn1 and Mn2, respectively [2], which are significantly smaller than expected 5 Bohr magneton. The reduced magnetic moments suggest partial cancellation by the COC orbital magnetic moments. We infer that the upper limit of the COC orbital magnetic moments is on the order of 0.10 Bohr magneton. We are mindful

that it is always possible that the Mn local moments could be smaller than expected, thus less cancellation with the COC orbital magnetic moments would be needed to produce the total observed moments.

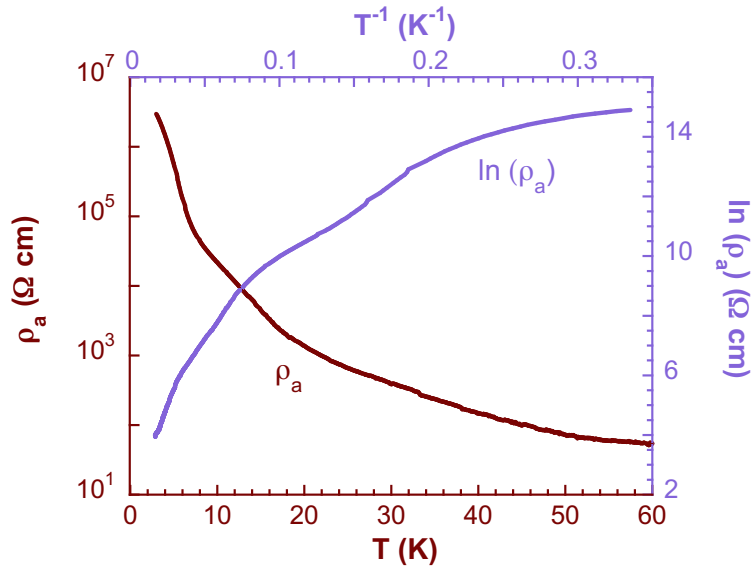
6. The magnetostriction is associated with the COC orbital moments because the Lorentz force acts to expand an *ab*-plane COC circulating on the rigid Te-Te edges of MnTe₆ octahedra when $H \parallel c$ -axis. The net orbital magnetization, which equals the loop current times the orbital area, naturally increases due to increasing the orbital area.
7. The S-shaped negative differential resistance is uncommon in bulk materials, it highly desirable for nonvolatile memory devices [3, 4].
8. The rigid coupling of the COC to the Te sublattice and M_{Mn} is a signature of the new state. The COC extend over multiple atomic sites, with couplings that depend on the ionic positions and dictate the current strength. The strong coupling sets time scales, which enables the COC state to remain metastable over seconds or minutes before undergoing a first-order transition to a trivial state when applied DC currents exceed certain critical values (on the order of 1 mA). Such a long-time scale is rare, if not unprecedented, but understandable. In the main text, we infer that this transition may mimic an ice-to-water phase transition. During ice melting, the thermal energy is spent to break the stiff hydrogen bonds, without raising temperature. The temperature of the system rises abruptly only when all hydrogen bonds are broken, i.e., the ice is completely melted. An analogy drawn here is that at the metastable state or during the COC melting, the applied DC currents (on the order of 1 mA) circulate in the sample to break COC in every unit cell, without causing a voltage or resistance increase before all COC are completely melted. This is because electrons always flow along the least resistive path, and this case, the remaining COC, according to the two-channel model. Breaking the

COC inevitably causes rearrangements of Te orbitals and atoms, more generally, changing lattice properties, therefore a long delay for switching. The larger the applied currents, the faster they can destroy all COC, thus a shorter time delay.

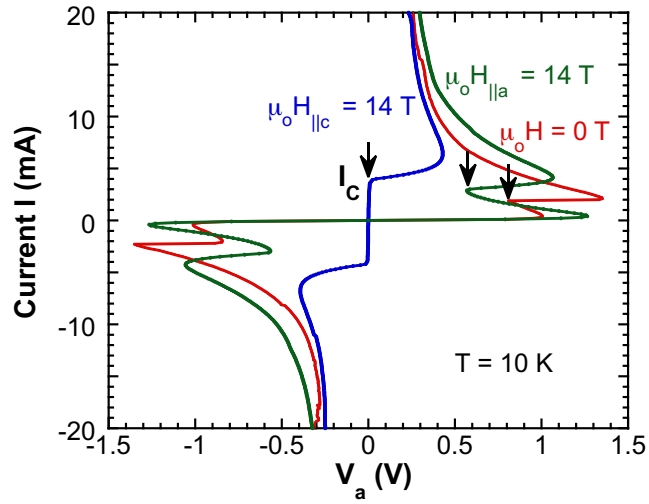
II. Experimental details

Single crystals of $\text{Mn}_3\text{Si}_2\text{Te}_6$ were grown using a flux method [29]. Measurements of crystal structures were performed using a Bruker Quest ECO single-crystal diffractometer with an Oxford Cryosystem providing sample temperature environments ranging from 80 K to 400 K. Chemical analyses of the samples were performed using a combination of a Hitachi MT3030 Plus Scanning Electron Microscope and an Oxford Energy Dispersive X-Ray Spectroscopy (EDX). The measurements of the electric resistivity and I-V characteristic were carried out using a Quantum Design (QD) Dynacool PPMS system having a 14-Tesla magnet and a set of external Keithley meters that provides current source and measures voltage with a high precision. The magnetization with electric current was measured using a Quantum Design MPMS-XL magnetometer with a homemade probe. The magnetostriction was measured using a home-made dilatometer compatible with the QD Dynacool PPMS system. The dilatometer is made with four identical KYOWA, type KFL strain gauges forming a Wheatstone bridge with the sample mounted on one arm and the rest three as compensators to cancel unwanted changes in the strain gauges due to changes in temperature and/or magnetic field.

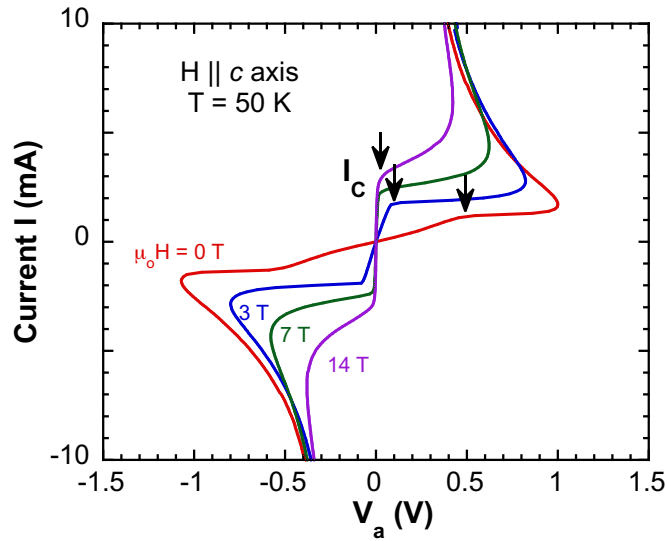
III. Additional data



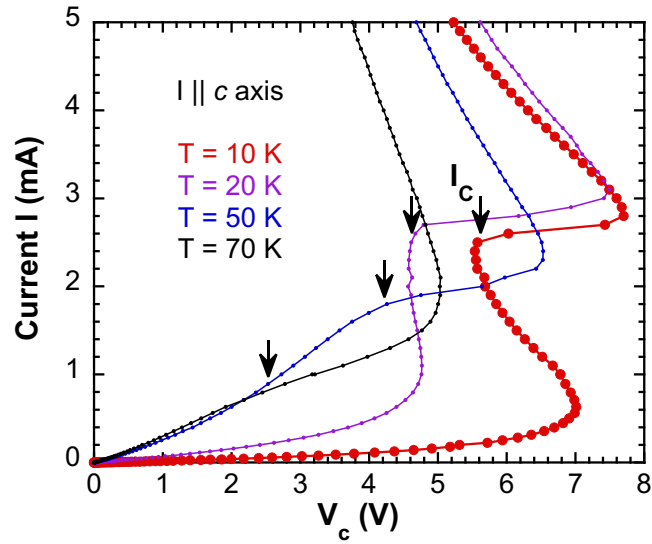
SM-Fig.2. Resistivity at low temperatures: The temperature dependence of the a -axis resistivity ρ_a at low temperatures (data in brown), and $\ln(\rho_a)$ vs. T^{-1} (data in light purple). Note that ρ_a does not follow an activation law and or a simple power law at low temperatures.



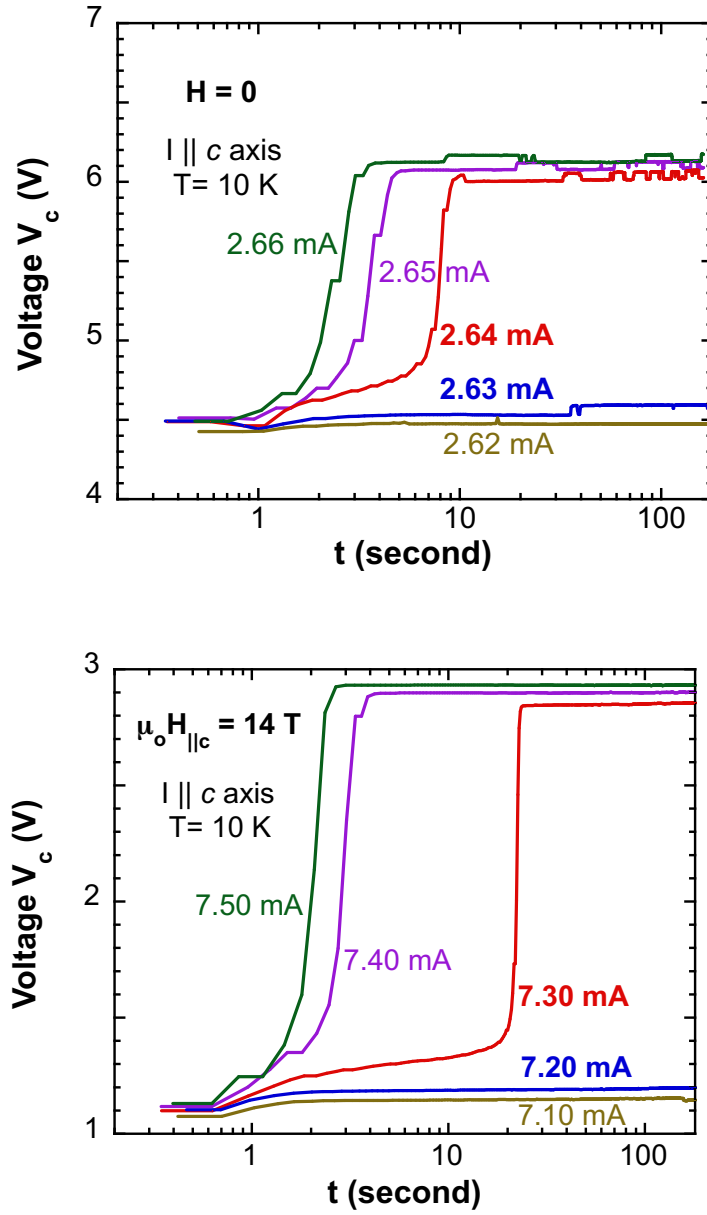
SM-Fig.3. Comparison of the I-V characteristic at $H \parallel a$ -axis and $H \parallel c$ -axis: The a -axis I-V characteristic at 10 K for $H = 0$ (red), $\mu_0 H = 14$ T along the a -axis (green) and the c -axis (green). Note the regime where $\Delta V/\Delta I = 0$ emerges only when $H \parallel c$ -axis.



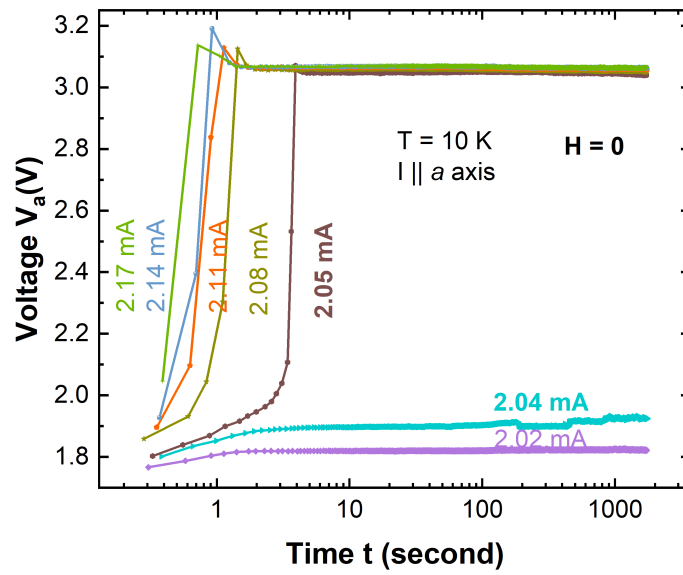
SM-Fig.4. The I-V characteristic at $H \parallel c$ -axis and 50 K: Note the regime $\Delta V/\Delta I = 0$ persists at 7 T and 14 T.



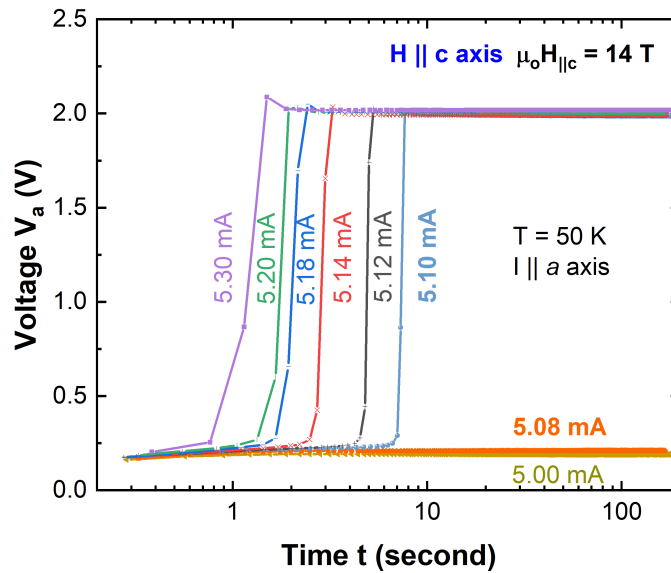
SM-Fig.5. The I-V characteristic at $I \parallel c$ -axis for various temperatures: Note that the I-V characteristic is qualitatively similar to that for $I \parallel a$ -axis but the first-order switching at I_c is weaker.



SM-Fig.6. Time-dependent bistable switching for current applied along the c -axis at 10 K for $H = 0$ (upper panel) and $\mu_0 H = 14$ T (lower panel).



SM-Fig.7. Time-dependent bistable switching at 10 K with 1,800 seconds elapsed.



SM-Fig.8. Time-dependent bistable switching at 50 K and $\mu_0 H_{\parallel c} = 14 \text{ T}$

IV. Additional discussion on chiral orbital currents

Below T_C , the ferrimagnetic order is observed with magnetic symmetry group $C2'/c'$ (No. 15.89, BNS setting) [2]. This symmetry group allows certain configurations of Te orbital currents circulating within the unit cell. Since we are particularly interested in the COC configurations with c -axis orbital moments, we focus on one particular subset of COC patterns that respect not only the magnetic group 15.89, but also the additional 3-fold rotational symmetry inherited from the full crystal space group $P-31c$ (No. 163). There are four independent current patterns that preserve this combination of 15.89 plus 3-fold rotations. The resulting four-parameter COC state is depicted in **Figs. 5a-5c** in the main text.

This symmetry-preserving COC state Ψ_C yields currents circulating on octahedral top/bottom faces as well as around Mn sites and around the Si sites. The resulting magnetic moments are all oriented exactly along the c -axis and can produce a nonzero net c -axis moment. There are four additional independent current patterns that preserve the magnetic group 15.89 but break 3-fold rotation symmetry; these patterns, denoted Ψ_a , are described below, and produce moments oriented within the ab -plane, coupling only weakly to c -axis fields. Henceforth we focus on Ψ_C , which gives the primary contribution to the COC state and its response to c -axis fields.

The COC of Ψ_C circulate along Te-Te octahedra edges and primarily involve Te orbitals. The Mn local moment pattern detected in neutron scattering [2] linearly couples to the order parameter of Ψ_C in a Landau-Ginzburg theory. Therefore, the orbital currents and localized moments both contribute to the observed magnetic pattern and cannot be fully distinguished. As such, Ψ_C can be viewed as a superposition of Mn and Te states that forms time-reversal-breaking multi-site molecular orbitals.

Application of $H \parallel c$ -axis couples to Ψ_C via the c -axis orbital moments, which in turn drastically enhances the COC order parameter, therefore the hopping matrix elements, and accommodates more current passing through the sample (**Fig. 5a** in the main text), leading to the observed CMR. Clearly application of $H \parallel a$ -axis weakens the c -axis orbital moments, thus reducing Ψ_C , and necessarily causes suppression of the CMR. On the other hand, applying uniform current $I > 2\text{mA}$ (along the a or c axes) weakens the COC order parameter, therefore destabilizes Ψ_C in favor of the trivial state Ψ_T . This is expected since the COC configuration does not permit any net current because each of the four independent parameters that specify Ψ_C forms a circulating current within the unit cell with no net uniform component (**Figs. 5a-5c** in the main text). The resistivity is reduced with increased I ; but at the same time, the increased I also weakens and eventually suppresses the ferrimagnetic state, and consequently Ψ_C , leading to a first-order phase transition that destroys the COC state (**Figs. 2a-2d** in the main text).

Strong electron-lattice coupling is an important feature of Ψ_C . The COC extend over multiple atomic sites, with couplings that depend on the ionic positions in the lattice and determine the current strengths. Therefore, Ψ_C entails a much stronger coupling between the lattice and the c -axis magnetic moments, and associated anisotropic magnetoelastic coupling, compared to that due to conventional Mn^{+2} -site, spin-only moments. This property of Ψ_C is consistent with the large magnetostriction $\Delta a/a$ when $H \parallel c$ -axis and the nearly negligible $\Delta a/a$ when $H \parallel a$ -axis (**Fig. 1c** in the main text). Note that these effects occur only below T_C where Ψ_C exists.

The strong coupling of COC to the lattice suggests that the current-driven transition from the COC to the trivial state should be strongly first order as observed (**Figs. 1-4** in the main text). The long-time scale (seconds or minutes) for the bistable switching is consistent with a picture wherein melting Ψ_C involves changing lattice properties (e.g., bond lengths or fluctuations/phonon

effects), thus allowing Ψ_C to remain metastable over long time scales set by *ionic motion* rather than just by electrons and/or Mn spins. The coupling between Ψ_C and the lattice increases when $H \parallel c$ -axis, thus the observed longer time delay, but significantly weakened when $H \parallel a$ -axis, leading to a mixed state with coexisting Ψ_C and Ψ_a .

V. Additional symmetry discussion

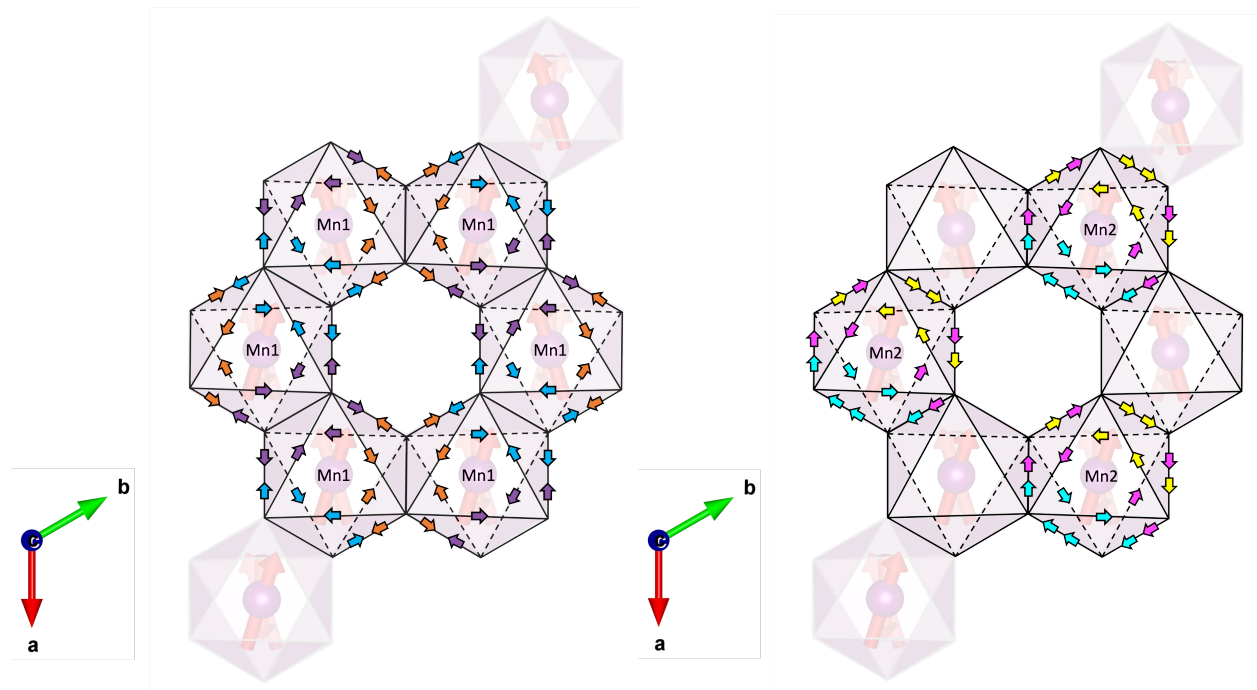
As depicted in **Fig. 5** of the main text, Ψ_C respects both (1) a lower monoclinic magnetic space group $C2'/c'$ (No. 15.89, BNS setting) which correctly describes the canted magnetic structure [26], and (2) an extra 3-fold rotational symmetry about the c -axis endowed from the full crystal space group $P-31c$ (No. 163). Additional COC are symmetry allowed by (1), but they do not couple as strongly to applied fields in the c -axis. These additional COC are shown in **SM-Fig. 9** and parametrize the state Ψ_a .

The full COC state is parametrized by eight independent COC. These include three of the COC of Ψ_C which have c -axis moments (red, blue, green in **Fig. 5** in the main text) and the six COC shown in **SM-Fig. 9** which do not constitute a linearly independent set of COC. One of COC (purple in **Fig. 5**) is in fact a linear combination of COC that circulate around Mn1 atoms (**SM-Fig. 9** (left)) and different COC from Ψ_C (blue in **Fig. 5**).

The sum of the three COC circulating about Mn1 atoms (**SM-Fig. 9** (left)) in equal magnitudes in fact gives the difference of two COC of Ψ_C (red minus blue in **Fig. 5** in the main text). Moreover, the sum of the three COC in equal magnitudes circulating about the Mn2 atoms (**SM-Fig. 9** (right)) gives another difference of two COC of Ψ_C (blue minus twice purple). These linear combinations are symmetry allowed by the 3-fold rotational symmetry described above. In total, the COC state thus has the four parameters of Ψ_C , six additional parameters symmetry allowed by the magnetic

space group, and two constraints relating the ten parameters. Indeed, the full COC state is thus parametrized by eight independent COC.

The unit vector normal to the plane about which each COC circulates in Ψ_C is exactly along the c -axis. The COC of this state clearly couple most strongly to applied fields in the c -axis. In contrast, the COC of Ψ_a do not couple strongly to applied fields in the c -axis. Instead, the orbital moments generated by the COC in the Mn1 plane point primarily in the ab -plane, and they are (approximately) pairwise separated by 120° . Their orientation is slightly nontrivial since the MnTe_6 octahedra are not regular octahedra. The orbital moments generated by the COC in the Mn2 plane similarly are not well aligned with the c -axis, and their orientation is also nontrivial.



SM-Fig. 9. Chiral orbital current parameters of Ψ_a in the Mn1 (left) and Mn2 (right) planes:

Three independent currents (orange, purple, and cerulean) run along Te-Te bonds in the Mn1 plane (left) and are symmetry allowed magnetic space group. Three more independent currents (cyan, magenta, and yellow) run along Te-Te bonds in the Mn2 plane (right). These currents are not linearly independent of the COC of **Fig. 5** of the main text. Explicitly, the sum of the orange,

purple, and cerulean COC (left) gives the difference of the red and blue COC of **Fig. 5** in the main text. Moreover, the sum of the cyan, magenta, and yellow COC (right) gives the difference of the blue and twice purple COC of **Fig. 5**. Bonds with two arrows of the same color indicate that the current magnitude is doubled on that edge. In total, the COC state is parametrized by eight independent loop currents.

References

1. *Colossal angular magnetoresistance in ferrimagnetic nodal-line semiconductors*, J. Seo, C. De, H. Ha, J. E. Lee, S. Park, J. Park, Y. Skourski, E. S. Choi, B. Kim, G. Y. Cho, H. W. Yeom, S.-W. Cheong, J. H. Kim, B.-J. Yang, K. Kim, and J. S. Kim, *Nature* **599**, 576 (2021)
2. *Magnetic Structure and Spin Fluctuation in Colossal Magnetoresistance Ferrimagnet $Mn_3Si_2Te_6$* , Feng Ye, Masaaki Matsuda, Zachary Morgan, Todd Sherline, Yifei Ni, Hengdi Zhao, and Gang Cao, submitted to *Phys. Rev. B Letters*, 2022
3. *Emerging memories: resistive switching mechanisms and current status*, Doo Seok Jeong, Reji Thomas, R S Katiyar, J F Scott, H Kohlstedt, A Petraru and Cheol Seong Hwang, *Rep. Prog. Phys.* **75**, 076502 (2012)
4. *Who Wins the Nonvolatile Memory Race?* G.I. Meijer, *Science* **319**, 1625 (2008)